



1 Break in precipitation – temperature scaling over India 2 predominantly explained by cloud-driven cooling

3 Sarosh Alam Ghausi^{1,2}, Subimal Ghosh^{3,4} and Axel Kleidon¹
4
5

6 ¹ Biospheric Theory and Modelling Group, Max Planck Institute for Biogeochemistry, Jena 07745,
7 Germany.

8 ² International Max Planck Research School for Global Biogeochemical Cycles (IMPRS – gBGC), Jena
9 07745, Germany

10 ³ Department of Civil Engineering, Indian Institute of Technology Bombay 400076, India

11 ⁴ Interdisciplinary Programme in Climate Studies, Indian Institute of Technology Bombay 400076, India

12 *Correspondence to:* Sarosh Alam Ghausi (sghausi@bgc-jena.mpg.de)
13

14 **Abstract.** Climate models predict an intensification of precipitation extremes as a result of a warmer and
15 moister atmosphere at the rate of 7%/K. However, observations in tropical regions show contrastingly
16 negative precipitation-temperature scaling at temperatures above 23° - 25°C. We use observations from
17 India and show that this negative scaling can be explained by the radiative effects of clouds on surface
18 temperatures. Cloud radiative cooling during precipitation events make observed temperatures co-vary
19 with precipitation, with wetter periods and heavier precipitation having a stronger cooling effect. We
20 remove this confounding effect of clouds from temperatures using a surface energy balance approach
21 constrained by thermodynamics. We then find a diametric change in precipitation scaling with rates
22 becoming positive and coming closer to the Clausius – Clapeyron scaling rate (7%/K). Our findings imply
23 that the intensification of precipitation extremes with warmer temperatures expected with global warming
24 is consistent with observations from tropical regions when the radiative effect of clouds on surface
25 temperatures and the resulting covariation with precipitation is accounted for.
26



27 **1 Introduction**

28 Climate models and observed trends have shown precipitation extremes to increase at the global scale
29 with anthropogenic global warming (Fischer et al., 2013; Westra et al., 2013; Donat et al., 2016). This
30 increase is largely explained by the thermodynamic Clausius-Clapeyron (CC) equation, suggesting a
31 $\approx 7\%/K$ increase in atmospheric moisture holding capacity per degree rise in temperature ("CC rate")
32 (Allen & Ingram, 2002). Extreme precipitation is expected to increase at a similar rate (Trenberth et al.,
33 2003; Held & Soden., 2006; O’Gorman & Schneider, 2009), as also shown by convection-permitting
34 climate model projections (Kendon et al., 2014; Ban et al., 2015). Precipitation – temperature scaling
35 rates, estimated using statistical methods and observed records, are widely used as an indicator to
36 constrain this response (Lenderink et al., 2008; Wasko et al., 2014).

37
38 However, observed scaling rates show large heterogeneity globally, with significant deviations from the
39 CC rate (Westra et al., 2014; Schroerer & Kirchengast, 2018). Deviations are larger in the tropical regions
40 where scaling rates are mostly negative and precipitation extremes largely show a monotonic decrease or
41 a sudden drop (hook) in scaling at high temperatures (Utsumi et al., 2011). These deviations have been
42 studied and attributed to number of factors. Two primarily argued reasons include the moisture
43 availability limitation at high temperatures (Hardwick et al., 2010) and dependence of scaling estimates
44 on the wet event duration (Gao et al., 2018; Ghausi & Ghosh 2020; Visser et al., 2021). Cooling effects
45 of rainfall events have also questioned the use of surface air temperature as scaling variable (Bao et al.,
46 2017). Other scaling variables like atmospheric air temperature (Golroudbary et al., 2019), sampling
47 temperatures before the start of storm (Visser et al., 2020), using measures of atmospheric moisture like
48 dew point temperature (Bui et al., 2019) and integrated water vapor (Roderick et al., 2019) have been
49 suggested as an alternative to surface air temperatures. The use of atmospheric moisture as a scaling
50 variable has been criticized because it provides less insight about precipitation sensitivity to temperature
51 and is also not entirely immune to cooling effects of rainfall (Bao et al., 2018). Other factors that can
52 cause deviations in scaling includes the change in rainfall type from stratiform to convective (Berg et al.,
53 2013; Molnar et al., 2015) and seasonality in precipitation (Sun et al., 2020). Owing to these uncertainties,



54 the use of scaling relationships derived from observations to infer future changes in extreme precipitation
55 in these regions remains debatable.

56

57 Here we show that a large part of uncertainties in this response and negative scaling rates in the tropics
58 are mainly caused by the radiative effect of clouds on surface temperatures. Precipitation events are
59 accompanied by strong cloud cover, which reduces the solar absorption at the surface and hence lowers
60 surface temperatures. This radiative cooling associated with precipitation can be significant in the tropical
61 regions where insolation and temperatures are high. As a result, regions and periods of more intense
62 precipitation cool more, and this affects their position in the scaling curve. This implies that temperature
63 observations are not independent of precipitation and this dependency obscures their scaling relationship.
64 Here we used a thermodynamic systems approach to remove this cooling effect from surface
65 temperatures. We then show that when this effect is being removed, no breakdown in the scaling
66 relationship is seen in observations and extreme precipitation then scales positively with temperature
67 close to CC rate.

68

69 To remove the effects of clouds, we used a surface energy balance formulation in conjunction with the
70 first and second law of thermodynamics (Kleidon & Renner, 2013). This approach provides us with
71 additional thermodynamic constraints on the turbulent flux exchange between surface and atmosphere.
72 We used this thermodynamically constrained model and force it with the “all-sky” and “clear-sky”
73 radiative fluxes. These fluxes are a standard product in NASA-CERES radiation datasets such that “all-
74 sky” fluxes are representative of observed conditions including the cloud effects while “clear-sky” fluxes
75 are diagnosed by removing the effect of clouds from the radiative transfer. Compounding the
76 thermodynamic constraint on turbulent fluxes together with the radiative fluxes helps us to estimate “all-
77 sky” and “clear-sky” temperatures that includes and excludes the radiative effects of clouds respectively.

78

79 We then evaluate this effect and its impact on precipitation-temperature scaling using observations from
80 India. India is a tropical country where the extreme precipitation and the resulting floods have intensified
81 over the past years (Goswami et al., 2006) and are expected to increase in the future (Katzenberger et al.,



2021). However, extreme precipitation–temperature scaling is largely negative over most of India (Vittal et al., 2016; Sharma et al., 2019), which is in contrast to the observed trends (Roxy et al., 2017). We here attempt to resolve this inconsistency in precipitation – temperature scaling by removing the cloud cooling effects from surface temperatures. To do this, we use gridded precipitation – temperature datasets that were used in previous studies (Vittal et al., 2016; Mukherjee et al., 2018; Sharma et al., 2019; Ghausi et al., 2020) and supplement it with the gridded radiative flux datasets to remove the cloud radiative effects. More details on our surface energy-balance model and estimation of surface temperatures “with” and “without” clouds are followed in the section 2.1 with the details of datasets being used in section 2.2. We used these reconstructed temperatures to study the effect of clouds on precipitation – temperature scaling over India. To estimate the precipitation – temperature scaling rates, we used the widely adopted statistical methods. Details of them are further provided in section 2.3. Results are then presented and discussed in section 3.

2 Methods and Data

2.1 Thermodynamically constrained energy balance model

To infer surface temperatures from the radiative forcing and remove the effects of clouds, we start with a simple physical formulation of the surface energy balance. The surface of the Earth is heated by solar absorption and downwelling longwave radiation. This heat is released back to the atmosphere through surface emission of longwave radiation and exchange of turbulent fluxes of sensible and latent heat. This balance between the incoming and outgoing energy fluxes at the Earth’s surface is described by the equation (1).

$$R_s + R_{ld} = R_{l,up} + J \quad (1)$$

Here R_s is the surface net solar absorption, R_{ld} is the downwelling longwave radiation, $R_{l,up}$ is the upwelling longwave radiation emitted from the surface and J is turbulent flux exchange between surface and the atmosphere (comprising of sensible and latent heat). We neglect the ground heat flux, as it is generally small when averaged over a few days or longer. While R_s and R_{ld} can be obtained using radiation datasets for different sky conditions, the partitioning between $R_{l,up}$ and J is poorly constrained by surface energy balance alone. To have these additional constraints on J , we used a thermodynamic systems



09 approach to view the earth system. Similar approach had also been used in (Kleidon & Renner, 2013;
10 Kleidon et al., 2014; Dhara et al., 2016) and were found to very well capture the observed surface
11 temperatures, energy partitioning and climate sensitivities.

12 To do this, we conceptualize the surface atmosphere system as a heat engine, with warm Earth surface as
13 the heat source and cooler atmosphere being the sink (Figure 1). Heat and mass are transported within
14 this engine by the exchange of turbulent fluxes (J) between the surface and the atmosphere. The
15 differential radiative heating and cooling between the surface and the atmosphere maintains the
16 temperature difference and drives the vertical convective motion. The power (G) associated with the work
17 done by the heat engine required to sustain convective motion in form of vertical mixing and exchange
18 of turbulent fluxes can be derived simply using the first and second law of thermodynamics and can be
19 represented by the well-established Carnot limit as

$$20 \quad G = J \left(1 - \frac{T_a}{T_s} \right). \quad (2)$$

21 Detailed derivation about the same can be found in (Kleidon & Renner, 2013; Kleidon et al., 2014). Here
22 T_a and T_s are the representative temperatures of cold atmosphere and the hot surface respectively.

23 Both temperatures are inferred from their respective energy balances. The atmospheric temperature (T_a)
24 is assumed to be equal to the radiative temperature of atmosphere and is estimated using the outgoing
25 longwave radiation at top of atmosphere ($R_{l,toa}$)

$$26 \quad T_a = \left(\frac{R_{l,toa}}{\sigma} \right)^{1/4}. \quad (3)$$

27 Here, σ is the Stefan Boltzmann constant ($\sigma = 5.67 \times 10^{-8} \text{ Wm}^{-2}\text{K}^{-4}$). A correction of 15K was applied to
28 the radiative temperature to account for the assumption of black atmosphere and effective height of
29 convection (Dhara et al., 2016). We consider the atmosphere as opaque to terrestrial radiation and hence
30 it is assumed that all outgoing longwave radiation emitted into space originates from the atmosphere.

31 The heat engine source temperature i.e. surface temperature (T_s) can be expressed from the emitted
32 longwave radiation from the surface ($R_{l,up}$) as

$$33 \quad T_s = \left(\frac{R_{l,up}}{\sigma} \right)^{1/4}. \quad (4)$$



34 Using the surface energy balance (Eq. 1), we can then express the surface temperature in terms of net
35 solar absorption, downwelling longwave radiation and turbulent fluxes (J) as

$$36 \quad T_s = \left(\frac{R_s + R_{ld} - J}{\sigma} \right)^{1/4}. \quad (5)$$

37 The differential radiative heating and cooling between the surface and the atmosphere maintains the
38 temperature difference and drives the vertical convective motion. Thermodynamics sets a limit to this
39 conversion and thus constrains the amount of turbulent flux exchange. Less turbulent fluxes result in a
40 hotter surface (Eq. 5), which will increase the temperature difference between the surface and atmosphere.
41 This will subsequently increase the efficiency term in the generation rate, the second term on the right-
42 hand side of Eq. (2). On the other hand, an increase in turbulent fluxes (J) increases the first term in the
43 generation rate of Eq. (2), but it will, in turn, reduce the surface temperature and temperature difference
44 between surface and atmosphere (Eq. 5). Thus, there exists a trade-off that sets the limit for the power to
45 maintain vertical energy and mass exchange between surface and the atmosphere. This limit is termed as
46 the maximum power limit and provides an additional constraint to surface energy balance partitioning
47 that we used here to infer surface temperatures.

48 Using Equations. (2), (3) and (5), the rate of work done (power) produced by the heat engine can be
49 expressed as a function of turbulent fluxes (J) as

$$50 \quad G = J \left(1 - T_a \left(\frac{R_s + R_{ld} - J}{\sigma} \right)^{-1/4} \right). \quad (6)$$

51 Note that power $G = 0$ when $J = 0$ or when $J = R_s + R_{ld} - R_{l,toa}$. Hence, there is a maximum $G_{max} = G$
52 ($J_{maxpower}$) for a value between $0 < J_{maxpower} < R_s + R_{ld} - R_{l,toa}$. The optimum J that maximizes power was
53 calculated numerically. This flux was then used to determine the surface temperatures.

$$54 \quad T_{s,maxpower} = \left(\frac{R_s + R_{ld} - J_{maxpower}}{\sigma} \right)^{1/4} \quad (7)$$

55 Surface temperatures were estimated using Eq. 7 for “all-sky” and “clear-sky” radiative conditions using
56 radiative forcing from the NASA – CERES datasets. We then refer to these two temperatures derived
57 using Eq. 7 as “all-sky” and “clear-sky” temperatures.

58

59



60 **2.2 Datasets used**

61 Radiative fluxes of shortwave and longwave radiation at surface and top of atmosphere (TOA) were
62 obtained from the NASA - CERES (EBAF 4.1) dataset (Loeb et al., 2018; Kato et al., 2018) and NASA
63 CERES Syn1deg dataset (Doelling et al., 2013,2016). These datasets are available for both “all-sky” as
64 well as “clear-sky” conditions at monthly and daily scale respectively with a 1° latitude x 1° longitude
65 spatial grid resolution and were used as a forcing in our energy balance model. We evaluated our model
66 using observations derived gridded temperature data from Indian Meteorological Department (IMD,
67 Rajeevan et al., 2008). To estimate the precipitation – temperature scaling, we used daily gridded
68 precipitation and temperature datasets with a spatial resolution of 1° latitude x 1° longitude from the
69 Indian Meteorological Department (IMD, Rajeevan et al., 2008) and 3 hourly gridded rainfall data from
70 NASA-TRMM_3B42 with a spatial resolution of 0.25° x 0.25°. We repeated the analysis using daily
71 gridded precipitation and temperature data from the APHRODITE (Asian Precipitation Highly Resolved
72 Observational Data Integration towards Evaluation) dataset, available at a spatial resolution of 0.25° x
73 0.25° (Yatagai et al., 2012). To further ensure robustness of our results, we also used 3 station-based daily
74 precipitation – temperature observations in India (Mumbai Airport, Bangalore Airport and Chennai
75 Airport) from global surface summary of the day (GSOD) data provided by National Oceanic and
76 Atmospheric Administration (NOAA). Daily dew point temperatures were obtained from the ERA-5
77 reanalysis. Based on the availability of all datasets, the period of analysis was chosen from the years 2003
78 to 2015.

80 **2.3 Estimation of precipitation – temperature scaling rates**

81 Extreme precipitation events were scaled with observed, “all-sky” and “clear-sky” temperatures using
82 two widely adopted scaling approaches: The Binning Method (Lenderink et al., 2008) and Quantile
83 Regression (Wasko et al., 2014). For the binning method, we defined extreme precipitation events using
84 a threshold of 99th percentile precipitation contained at each grid cell. Precipitation – temperature pairs
85 were then divided into the increasing order of non-overlapping bins of 2 K width. Only those bins which
86 have at least 150 data points have been considered for the analysis (Utsumi et al., 2011). The median
87 value of each bin was then used to examine the variation of precipitation extremes with temperature. Bins



88 with temperature less than 3°C were discarded to remove the effects of freezing, thawing and snowfall.
89 To ensure that our results are not biased with the number of data points in each bin and bin sizes (which
90 may affect the nature of the scaling relationship), we further used the Quantile Regression method to
91 estimate the scaling rates.

92 Quantile regression estimates the conditional quantile of the dependent variable (in our case,
93 precipitation) over the given values of the independent variable (temperature). We first fitted a quantile
94 regression model between the logarithmic precipitation and temperature values at the target quantile of
95 99%

$$96 \quad \mathbf{Log}(P_i) = \beta_o^{99} + \beta_1^{99}(T_i) \quad . \quad (8)$$

97 Here P_i denotes the mean daily precipitation intensity and T_i is the daily mean temperature, and β_o^{99} and
98 β_1^{99} are the regression coefficients for the 99th quantile of precipitation. The slope coefficient β_1^{99} is then
99 exponentially transformed to estimate the scaling rate (α_1).

$$00 \quad \alpha_1 = 100 \cdot (e^{\beta_1^{99}} - 1) \quad (9)$$

01 The following methodology had been widely adopted to estimate the extreme precipitation – temperature
02 scaling in previous studies (Lenderink et al., 2008, 2010; Utsumi et al., 2011; Wasko et al., 2014; Schroeer
03 et al., 2018).

04 **3 Results and Discussion**

05 In this section, we first start by a quick evaluation of our thermodynamic approach by comparing the
06 estimated “all-sky” temperatures against observations. We then quantify the cloud radiative effects on
07 surface temperatures and check for its spatial consistency across regions. We then estimated precipitation
08 – temperature scaling rates by including and excluding the effect of clouds on surface temperatures. We
09 also used dew point temperature (a proxy measure for atmospheric moisture) as a scaling variable. Later,
10 we discuss our interpretation of scaling by excluding cloud effects from temperatures, its comparison with
11 the dew point scaling and its implications across regions.

12
13



14 **3.1: Evaluating the modelled temperatures**

15 “All-sky” temperatures were estimated using the daily observed radiative fluxes from CERES in
16 conjunction with surface energy partitioning constrained by maximum power (see Equation 7). We found
17 an extremely good agreement of these estimated temperatures when compared to surface temperature
18 observations over India with $R^2 > 0.9$ and $RMSE < 1.5$ K over most regions (Figure 2). This signifies that
19 our formulation strongly captures the surface temperature variation over India and thus validates our
20 approach. We then extend this for clear-sky conditions by forcing our model with “clear-sky” radiative
21 fluxes from CERES and estimating “clear-sky” temperatures. It is to note that “clear-sky” temperatures
22 are reconstructed temperatures estimated by removing the effect of clouds from radiative transfer.

23 **3.2: Estimating the cloud radiative cooling**

24 We used the difference between the “all-sky” and “clear-sky” temperatures as a measure to quantify the
25 effect of cloud-driven cooling during rainfall events. This cooling increases strongly with precipitation
26 across regions, resulting in a stronger reduction in surface temperature with greater precipitation (Figure
27 3a). This cooling is predominantly caused by the substantial reduction in absorbed solar radiation at the
28 surface for “all-sky” conditions compared to “clear-sky” conditions (Figure 3b). On the other hand,
29 changes in longwave radiation are comparatively small and largely remain insensitive to precipitation.
30 To examine the spatial consistency in precipitation variability and associated cooling, we isolated extreme
31 daily precipitation days over each grid. Figure 4a shows the mean magnitude of daily extreme
32 precipitation events over India. Figure 4b shows the cloud-cooling associated with these days. This
33 cooling effect of clouds and precipitation shows a clear, systematic variation across India. The cooling
34 effect is greater where precipitation rates are high. In contrast, in the more arid regions in the northwest
35 of India, the cooling effect almost disappears with low precipitation rates. Figure 4c further shows the
36 mean “all-sky” temperature during these days. We find that the heaviest events occur at a relatively lower
37 temperature as a result of stronger cooling. Figure 4d shows the mean number of rainfall days per year.
38 More rainy days implies more cloudy conditions and thus a stronger cloud radiative cooling over that
39 region. Having quantified this effect of cloud radiative cooling and its systematic variation across regions,
40 we then estimate its impact on the precipitation – temperature scaling.

41



42 **3.3 Impact on precipitation-temperature scaling**

43 We performed a binning analysis (Lenderink et al., 2008) to understand the scaling of precipitation
44 extremes with temperature using observed temperatures as well as our estimated "clear-sky" and "all-sky"
45 temperatures. Precipitation events were isolated and binned into P-T pairs and the resulting scaling
46 relationships are shown in Figure 5. The scaling relationship using observed and "all-sky" temperatures
47 showed similar scaling behaviour (yellow and red lines in Figure 5a). Extreme precipitation increases
48 close to the CC rate up to a threshold of around 23° - 24°C, above which the scaling becomes negative.
49 This break in scaling behaviour with observed temperatures is consistent with the findings of previous
50 studies (Hardwick et al., 2010; Ghausi & Ghosh, 2020) and is commonly referred in literature as "hook"
51 or "peak structure" (Wang et al., 2017; Gao et al., 2018). However, when precipitation extremes are scaled
52 with "clear-sky" temperatures that excludes the cloud-cooling effect, the resulting scaling relationship
53 does not show a breakdown and increases consistently, close to the CC rate over the whole temperature
54 range (blue line in Fig. 5a). Similar results were obtained when the scaling curves were reproduced for
55 station-based observations (See Appendix A).

56 Previous studies (Hardwick et al., 2010; Chan et al., 2015; Wang et al., 2017) have attributed the break
57 in precipitation-temperature scaling to a lack of moisture availability as relative humidity tends to
58 decrease at high temperatures. To account for this effect of moisture limitation, some studies used dew
59 point temperature, a measure of atmospheric humidity, as an alternative scaling variable (Wasko et al.,
60 2018; Barbero et al., 2018). They showed that the breakdown and negative scaling disappear when scaled
61 with dew point temperatures (Zhang et al., 2019; Ali et al., 2021). To evaluate this interpretation and
62 compare it to ours, we used the dew point temperature from the ERA-5 reanalysis. We derived the extreme
63 precipitation scaling using this temperature (Figure 5b) and compared it to our "all-sky" and "clear-sky"
64 temperatures (Figure 5c).

65 At first sight, the scaling relationship using dew point temperatures looks very similar to our "clear-sky"
66 relationship (compare Figures 5a and 5b, but note the difference in temperature scale). Yet, its
67 interpretation differs because using dew point temperatures merely implies that the intensity of extreme
68 precipitation events scales with the moisture content of the air, with moister air resulting in higher
69 intensity events. Dew point scaling thus carries less insight about the response of extreme precipitation to



70 climate warming (Bao et al., 2018). To infer the precipitation sensitivity with temperature from dew point
71 scaling, one then needs to see how dew point temperatures change with actual temperatures (dT_{dew}/dT)
72 (Figure 5c). This is further demonstrated using equation 10.

73

$$\frac{dP}{dT} = \frac{dP}{dT_{dew}} \times \frac{dT_{dew}}{dT} \quad (10)$$

74 If relative humidity remains unchanged, we would expect the dew point temperature to increase
75 continuously with surface temperature, representing a moisture increase of 7%/K. However, when dew
76 point temperatures are compared to "all-sky" temperatures (red line, Figure 5c), we note that a break
77 occurs in this scaling as well. Dew point temperatures increase with "all-sky" temperatures for colder
78 temperatures more strongly than what would be expected from an unchanged relative humidity when air
79 gets warmer. However, at temperatures of above 23° - 25°C, dew point temperatures fall, reflecting a
80 decrease in relative humidity that is typical for warm, arid regions. Thus, one does not see a breakdown
81 in precipitation - dew point scaling because the information on the breakdown is contained in how dew
82 point temperatures change with surface air temperatures (second term in equation 10). Similar findings
83 were also reported in Roderick et al (2019).

84 The scaling of dew point temperatures with "clear-sky" temperatures is much more uniform and consistent
85 across the whole temperature range and does not show a breakdown or a super CC scaling in the
86 relationship. This is because the "clear-sky" temperatures reflect the radiative conditions, and not the
87 effects of atmospheric humidity or clouds. In contrast, observed temperatures and "all-sky" temperatures
88 co-vary with cloud effects, which in turn are linked to precipitation and humidity, thus resulting in less
89 clear scaling relationships that are less straightforward to interpret. This further implies that moisture
90 loading of the atmosphere primarily occurs during the non-precipitating periods that are more
91 representative of clear-sky radiative conditions.

92 The breakdown in scaling effect can thus be explained by the cooler temperatures associated with
93 precipitation events. This cooling shifts the precipitation extremes to lower temperature bins while the
94 high-temperature bins then correspond to more arid regions or to the drier pre-monsoon season
95 temperatures with lower values of precipitation extremes. We refer to this as a "bin-shifting" effect. The
96 cooling effect is proportional to the amount of precipitation (Fig. 3A) and hence, the heavier the



97 precipitation, the stronger the cooling and bin shifting becomes. When the cloud cooling effect is
98 removed, as in the case of "clear-sky" temperatures, extreme precipitation then shows a scaling that is
99 consistent with the CC rate. This bin shifting effect arising due to the presence of clouds also causes a
00 decrease in relative humidity at higher temperatures. This effect can be seen by the stronger increase in
01 dewpoint temperatures below 25°C, and the decline above this temperature (Figure 5c). The breakdown
02 in scaling is thus not directly related to changes in aridity or moisture availability, but rather to the
03 radiative effect of clouds on surface temperature.

04 To demonstrate the implications of our interpretation for precipitation scaling across regions, we
05 estimated regression slopes of 99th percentile precipitation events for both sub-daily (TRMM) and daily
06 (IMD & APHRODITE) precipitation with the different temperatures using the Quantile Regression
07 method (Wasko et al., 2014). We found that extreme precipitation scaling was negative for both, observed
08 and "all-sky" temperatures over most regions (Figure 6) except for the Himalayan foothills in the North
09 of India. The scaling rates for sub-daily extremes were slightly higher than those estimated for daily
10 extremes but yet remains negative over most grids. When the cooling effect of clouds is removed by using
11 "clear-sky" temperatures, extreme precipitation scaling then shows a diametric change and scaling
12 estimates come close to CC rates over most of the regions. A similar diametric change in the scaling was
13 also obtained with the APHRODITE precipitation dataset (Appendix B).

14 We note that negative scaling was also found over few regions of South-central and south-east India with
15 "clear-sky" temperatures at both daily and sub-daily scales (Figure 6 c,f). To our understanding, this
16 negative scaling is largely due to the cyclonic activities originating from Bay of Bengal during winter
17 months and resulting in heavy rains over these regions. These cyclonic systems thus cause very high
18 rainfall at very low temperatures which causes negative scaling. More work is needed to be done to resolve
19 these systems in conventional scaling approach and remains an important area for future research.

20 The effect of seasonality on precipitation scaling was also checked by producing the scaling curves for
21 different seasonal subsets (summer and winter monsoon). Our findings indicate that seasonality does have
22 an effect on observed scaling while the "clear-sky" scaling rates remains positive irrespective of the
23 seasons (see Appendix C).



24 The confounding effect between precipitation and temperature on observed scaling relationships
25 “apparent scaling” had also been argued by some recent studies (Bao et al. 2017; Visser et al., 2020). Our
26 results agree with these studies that the observed scaling relationships also reflect the impact of synoptic
27 conditions and cooling associated with precipitation events on temperature. However, we suggest that this
28 confounding effect is largely associated with cloud radiative effect, which is removed by our use of “clear-
29 sky” temperatures as a scaling variable. We also address the arguments raised to resolve apparent scaling
30 using dew point temperature (Barbero et al., 2018). Our results confirm that precipitation extremes scale
31 well with dew point temperatures as a measure for atmospheric moisture, but that the break in scaling
32 actually originates from the scaling of dew point temperatures with observed temperatures. This response
33 of dew point temperature to warming is further affected by the presence of clouds and associated radiative
34 cooling. “Clear-sky” temperatures are independent of the co-variations arising from cloud effects and are
35 thus a better, more independent measure and scaling variable to understand the precipitation response to
36 climate warming.

37 **4 Summary and Conclusions**

38 We showed that the observed negative scaling of extreme precipitation in India arises mostly from the
39 cloud radiative cooling of surface temperatures. When this effect is removed, we get a positive scaling
40 consistent with the CC rate. Scaling rates estimated from observed temperatures are thus likely to
41 misrepresent the response of extreme precipitation to global warming, because the cooling effects of
42 clouds make precipitation and temperature covary with each other. When this effect is removed by
43 estimating surface temperatures for “clear-sky” conditions, the scaling relationships with moisture content
44 and precipitation become much clearer and confirm the CC scaling of extreme precipitation events with
45 warmer temperatures. This explains the apparent discrepancy between the observed negative scaling rates
46 over India and the projected increase in precipitation extremes by climate models.

47 It is also important to note that the goal of our study was not to compare the accuracy of scaling estimates
48 from different gridded and station-based datasets, but rather to identify and remove the physical effects
49 that causes uncertainties in this response. Our methodology to remove the cooling effect of clouds from
50 surface temperatures significantly improves the scaling estimate for daily precipitation scaling.



51 While our study was confined over the Indian region, we would expect that cloud effects on surface
52 temperatures can explain the deviations in precipitation scaling from CC rates in other tropical regions
53 too. Furthermore, our methodology to remove the cloud cooling effects on surface temperatures could be
54 extended to derive scaling relationships of other, observed variables to obtain their response to global
55 warming as well. Our findings add a novel component to better interpret precipitation scaling rates derived
56 from observations to support climate model projections.

57 **Data Availability**

58 The daily gridded precipitation and temperature datasets were obtained from the Indian Meteorological
59 department (IMD, https://cdsp.imdpune.gov.in/home_gridded_data.php (doi: 10.1029/2008GL035143)).
60 The APHRODITE (Asian Precipitation Highly Resolved Observational Data Integration towards
61 Evaluation) dataset is available at <http://aphrodite.st.hirosaki-u.ac.jp/products.html>. Sub-daily
62 precipitation data at 3 hourly resolution was obtained from TRMM (Tropical Rainfall measuring mission)
63 TMPA_3B42_V7 data (doi: 10.5067/TRMM/TMPA/3H/7)
64 https://disc.gsfc.nasa.gov/datasets/TRMM_3B42_7/summary. Station-based daily precipitation -
65 temperature data was taken from NOAA – GSOD sites (Station id: 43295099999, 43003099999 and
66 43279099999) at <https://www.ncei.noaa.gov/access/search/data-search/global-summay-of-the-day>.
67 Surface and TOA gridded radiative flux datasets are obtained from NASA CERES EBAF data (doi:
68 https://doi.org/10.5067/Terra-Aqua/CERES/EBAF_L3B.004.1) and NASA CERES Syn1deg data (doi:
69 10.5067/TERRA+AQUA/CERES/SYN1DEG-1HOUR_L3.004A) at <https://ceres.larc.nasa.gov/data/>.
70 Daily dew point temperature data is obtained from the ERA-5 reanalysis (doi: 10.24381/cds.e2161bac).

71 **Acknowledgements**

72 The author thanks the NASA CERES team for making the satellite data openly available (doi:
73 10.5067/Terra-Aqua/CERES/EBAF_L3B.004.1 and 10.5067/TERRA+AQUA/CERES/SYN1DEG-
74 1HOUR_L3.004A) and the Copernicus Climate Change Service for the access to the ERA-5 reanalysis
75 data (doi: 10.24381/cds.e2161bac).



76 **Author Contribution**

77 All the authors contributed to the idea and development of the hypothesis. SAG carried out the data
78 analysis. The writing of the manuscript was done by SAG with inputs and edits from AK. AK and SG
79 helped in designing the study. All the authors contributed to the interpretation of the results.

80 **References**

- 81 1. Acero, F., García, J., & Gallego, M. (2011). Peaks-over-Threshold Study of Trends in Extreme
82 Rainfall over the Iberian Peninsula. *Journal of Climate*, 24(4), 1089–1105. Retrieved May 31,
83 2021, from <http://www.jstor.org/stable/26190418>
- 84 2. Ali, H., Fowler, H. J., Lenderink, G., Lewis, E., & Pritchard, D. (2021). Consistent large-scale
85 response of hourly extreme precipitation to temperature variation over land. *Geophysical*
86 *Research Letters*, 48, e2020GL090317. <https://doi.org/10.1029/2020GL090317>
- 87 3. Allen, M., Ingram, W. Constraints on future changes in climate and the hydrologic cycle.
88 *Nature* 419, 228–232 (2002). <https://doi.org/10.1038/nature01092>
- 89 4. Ban, N., J. Schmidli, and C. Schär (2015), Heavy precipitation in a changing climate: Does
90 short-term summer precipitation increase faster?, *Geophys. Res. Lett.*, 42, 1165–1172,
91 [doi:10.1002/2014GL062588](https://doi.org/10.1002/2014GL062588).
- 92 5. Bao, J., Sherwood, S. C., Alexander, L. V. & Evans, J. P. Comments on “temperature-extreme
93 precipitation scaling: A two-way causality?”. *Int. J. Climatol.* 38, 4661–4663 (2018).
- 94 6. Bao, J., Sherwood, S., Alexander, L. et al. Future increases in extreme precipitation exceed
95 observed scaling rates. *Nature Clim Change* 7, 128–132 (2017).
96 <https://doi.org/10.1038/nclimate3201>
- 97 7. Barbero, R., Westra, S., Lenderink, G. & Fowler, H. J. Temperature-extreme precipitation
98 scaling: a two-way causality? *Int. J. Climatol.* 38, e1274–e1279 (2018).
- 99 8. Berg, P., Moseley, C., & Haerter, J. O. (2013). Strong increase in convective precipitation in
00 response to higher temperatures. *Nature Geoscience*, 6(3), 181–185.
01 <https://doi.org/10.1038/ngeo1731>



- 02 9. Bui A, Johnson F and Wasko C 2019 The relationship of atmospheric air temperature and dew
03 point temperature to extreme rainfall Environ. Res. Lett. 14 074025
- 04 10. Chan, S.C., Kendon, E.J., Roberts, N.M., Fowler, H.J. and Blenkinsop, S. (2015) Downturn
05 in scaling of UK extreme rainfall with temperature for future hottest days. Nature Geoscience,
06 9(1), 24– 28. <https://doi.org/10.1038/ngeo2596>.
- 07 11. Dhara, C., Renner, M., & Kleidon, A. (2016). Broad climatological variation of surface energy
08 balance partitioning across land and ocean predicted from the maximum power limit.
09 <https://doi.org/10.1002/2016GL070323.1>.
- 10 12. Doelling DR, Loeb NG, Keyes DF, Nordeen ML, Morstad D, Nguyen C, Sun M (2013)
11 Geostationary enhanced temporal interpolation for CERES flux products. J Atmos Oceanic
12 Technol 30(6):1072–1090
- 13 13. Doelling DR, Sun M, Nguyen LT, Nordeen ML, Haney CO, Keyes DF, Mlynchak PE (2016)
14 Advances in geostationary-derived longwave fluxes for the CERES synoptic (SYN1 deg)
15 product. J Atmos Oceanic Technol 33(3):503–521
- 16 14. Donat, M. G., Lowry, A. L., Alexander, L. V., O’Gorman, P. A. & Maher, N. More extreme
17 precipitation in the world’s dry and wet regions. Nat. Clim. Change 6, 508–513 (2016)
- 18 15. Fischer, E. M., Beyerle, U. & Knutti, R. Robust spatially aggregated projections of climate
19 extremes. Nat. Clim. Change 3, 1033–1038 (2013).
- 20 16. Gao, X., Zhu, Q., Yang, Z., Liu, J., Wang, H., Shao, W., & Huang, G. (2018). Temperature
21 Dependence of Hourly, Daily, and Event-based Precipitation Extremes Over China. Scientific
22 Reports, 8(1), 1–10. <https://doi.org/10.1038/s41598-018-35405-4>
- 23 17. Ghauri, S. A., & Ghosh, S. (2020). Diametrically Opposite Scaling of Extreme Precipitation
24 and Stream flow to Temperature in South and Central Asia, 1–10.
25 <https://doi.org/10.1029/2020GL089386>
- 26 18. Golroudbary, V. R., Zeng, Y., Mannaerts, C. M., & Su, Z. (2019). Response of extreme
27 precipitation to urbanization over the Netherlands. Journal of Applied Meteorology and
28 Climatology, 58(4), 645–661. <https://doi.org/10.1175/jamc-d-18-0180.1>



- 29 19. Goswami, B. N., Venugopal, V., Sengupta, D., Madhusoodanan, M. S. & Xavier, P. K. (2006).
30 Increasing trend of extreme rain events over India in a warming environment. *Science* 314,
31 1442–5. DOI: 10.1126/science.1132027
- 32 20. Hardwick Jones, R., Westra, S., & Sharma, A. (2010). Observed relationships between
33 extreme sub-daily precipitation, surface temperature, and relative humidity. *Geophysical*
34 *Research Letters*, 37(22), 1–5. <https://doi.org/10.1029/2010GL045081>
- 35 21. Held, I. M. and Soden, B. J.: Robust responses of the hydrological cycle to global warming, *J.*
36 *Climate*, 19, 5686–5699, 2006.
- 37 22. Kato, S., F. G. Rose, D. A. Rutan, T. E. Thorsen, N. G. Loeb, D. R. Doelling, X. Huang, W.
38 L. Smith, W. Su, and S.-H. Ham, 2018: Surface irradiances of Edition 4.0 Clouds and the
39 Earth’s Radiant Energy System (CERES) Energy Balanced and Filled (EBAF) data product,
40 *J. Climate*, 31, 4501-4527, doi:10.1175/JCLI-D-17-0523.1
- 41 23. Katzenberger, A.; Schewe, J.; Pongratz, J.; Levermann, A. Robust increase of Indian monsoon
42 rainfall and its variability under future warming in CMIP-6 models. *Earth Syst. Dyn.* 2020.
- 43 24. Kendon, E. J., Roberts, N. M., Fowler, H. J., Roberts, M. J., Chan, S. C., & Senior, C. A.
44 (2014). Heavier summer downpours with climate change revealed by weather forecast
45 resolution model. *Nature Climate Change*, 4(7), 570–576.
46 <https://doi.org/10.1038/nclimate2258>
- 47 25. Kleidon, A., & Renner, M. (2013). A simple explanation for the sensitivity of the hydrologic
48 cycle to climate change. *Earth System Dynamics*, 4(2), 455–465. [https://doi.org/10.5194/esd-](https://doi.org/10.5194/esd-4-455-2013)
49 [4-455-2013](https://doi.org/10.5194/esd-4-455-2013)
- 50 26. Kleidon, A., Renner, M., & Porada, P. (2014). Estimates of the climatological land surface
51 energy and water balance derived from maximum convective power. *Hydrology and Earth*
52 *System Sciences*, 18, 2201–2218. <https://doi.org/10.5194/hess-18-2201-2014>
- 53 27. Lenderink, G., & Van Meijgaard, E. (2008). Increase in hourly precipitation extremes beyond
54 expectations from temperature changes. *Nature Geoscience*, 1(8), 511–514.
55 <https://doi.org/10.1038/ngeo262>



- 56 28. Loeb, N. G., Doelling, D. R., Wang, H., Su, W., Nguyen, C., Corbett, J. G., Liang, L.,
57 Mitrescu, C., Rose, F. G., and Kato, S.: Clouds and the Earth's Radiant Energy System
58 (CERES) Energy Balanced and Filled (EBAF) Top-of-Atmosphere (TOA) Edition-4.0 data
59 product, *J. Climate*, 31, 895–918, <https://doi.org/10.1175/JCLI-D-17-0208.1>, 2018.
- 60 29. Molnar, P., Fatichi, S., Gaál, L., Szolgay, J., & Burlando, P. (2015). Storm type effects on
61 super Clausius-Clapeyron scaling of intense rainstorm properties with air temperature.
62 *Hydrology and Earth System Sciences*, 19(4), 1753–1766. [https://doi.org/10.5194/hess-19-](https://doi.org/10.5194/hess-19-1753-2015)
63 [1753-2015](https://doi.org/10.5194/hess-19-1753-2015)
- 64 30. Mukherjee S, Saran A, Stone D, Mishra V (2018) Increase in extreme precipitation events
65 under anthropogenic warming in India. *Weather Clim Extrem* 20:45–53.
66 <https://doi.org/10.1016/j.wace.2018.03.005>
- 67 31. O’Gorman, P. A. & Schneider, T. The physical basis for increases in precipitation extremes
68 in simulations of 21st-century climate change. *Proc. Natl Acad. Sci. USA* 106, 14773–14777
69 (2009).
- 70 32. Rajeevan, M., Jyoti Bhate, A.K.Jaswal : Analysis of variability and trends of extreme rainfall
71 events over India using 104 years of gridded daily rainfall data., , 2008, *Geophysical Research*
72 *Letters*, Vol.35, L18707, doi:10.1029/2008GL035143.
- 73 33. Roderick TP, Wasko C, Sharma A. 2019 Atmospheric moisture measurements explain
74 increases in tropical rainfall extremes. *Geophys. Res. Lett.* 46, 1375–1382.
75 (doi:10.1029/2018GL080833)
- 76 34. Roxy, M. K., Ghosh, S., Pathak, A., Athulya, R., Mujumdar, M., Murtugudde, R., ...
77 Rajeevan, M. (2017). A threefold rise in widespread extreme rain events over central India.
78 *Nature Communications*, 8(1), 1–11. <https://doi.org/10.1038/s41467-017-00744-9>
- 79 35. Schroeer, K., & Kirchengast, G. (2018). Sensitivity of extreme precipitation to temperature:
80 the variability of scaling factors from a regional to local perspective. *Climate Dynamics*,
81 50(11), 3981–3994. <https://doi.org/10.1007/s00382-017-3857-9>



- 82 36. Sharma, S., & Mujumdar, P. P. (2019). On the relationship of daily rainfall extremes and local
83 mean temperature. *Journal of Hydrology*, 572(September 2018), 179–191.
84 <https://doi.org/10.1016/j.jhydrol.2019.02.048>
- 85 37. Sun, Q., Zwiers, F., Zhang, X. & Li, G. A comparison of intra-annual and long-term trend
86 scaling of extreme precipitation with temperature in a large-ensemble regional climate
87 simulation. *J. Clim.* 33, 9233–9245 (2020).
- 88 38. Trenberth, K. E., Dai, A., Rasmussen, R. M., & Parsons, D. B. (2003). The changing character
89 of precipitation. *Bulletin of the American Meteorological Society*, 84(9), 1205–1217+1161.
90 <https://doi.org/10.1175/BAMS-84-9-1205>
- 91 39. Utsumi, N., Seto, S., Kanae, S., Maeda, E. E., & Oki, T. (2011). Does higher surface
92 temperature intensify extreme precipitation? 38(June), 1–5.
93 <https://doi.org/10.1029/2011GL048426>
- 94 40. Visser, J. B., Wasko, C., Sharma, A., & Nathan, R. (2020). Resolving Inconsistencies in
95 Extreme Precipitation-Temperature Sensitivities. *Geophysical Research Letters*, 47(18),
96 e2020GL089723. <https://doi.org/10.1029/2020GL089723>
- 97 41. Visser, Johan B., Conrad Wasko, Ashish Sharma, and Rory Nathan. "Eliminating the “Hook”
98 in Precipitation–Temperature Scaling", *Journal of Climate* 34, 23 (2021): 9535-9549, accessed
99 Nov 10, 2021, <https://doi.org/10.1175/JCLI-D-21-0292.1>
- 00 42. Vittal, H., Ghosh, S., Karmakar, S. et al. Lack of Dependence of Indian Summer Monsoon
01 Rainfall Extremes on Temperature: An Observational Evidence. *Sci Rep* 6, 31039 (2016).
02 <https://doi.org/10.1038/srep31039>
- 03 43. Wang, G., Wang, D., Trenberth, K. et al. The peak structure and future changes of the
04 relationships between extreme precipitation and temperature. *Nature Clim Change* 7, 268–274
05 (2017). <https://doi.org/10.1038/nclimate3239>
- 06 44. Wasko, C., & Sharma, A. (2014). Quantile regression for investigating scaling of extreme
07 precipitation with temperature. *Water Resources Research*, 50(4), 3608–3614.
08 <https://doi.org/10.1002/2013WR015194>

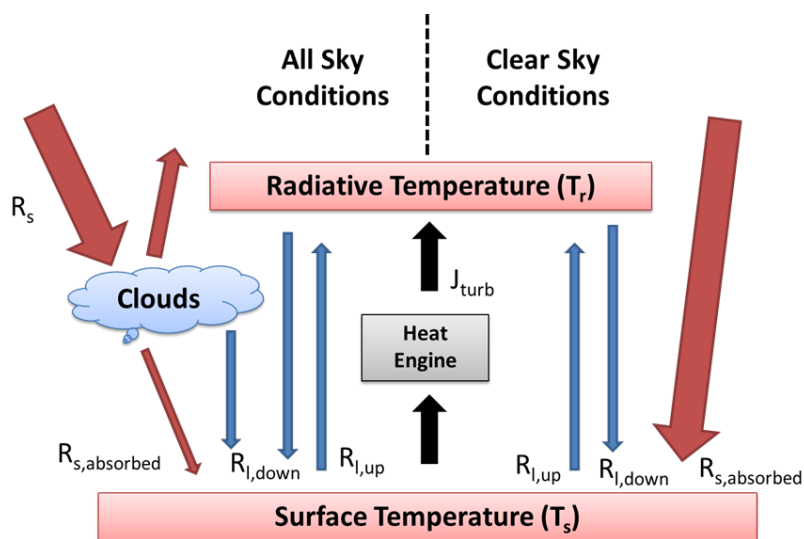


- 09 45. Wasko, C., Lu, W. T., & Mehrotra, R. (2018). Relationship of extreme precipitation, dry-bulb
10 temperature, and dew point temperature across Australia. *Environmental Research Letters*,
11 13(7). <https://doi.org/10.1088/1748-9326/aad135>
- 12 46. Westra, S., Alexander, L. V., & Zwiers, F. W. (2013). Global increasing trends in annual
13 maximum daily precipitation. *Journal of Climate*, 26(11), 3904–3918.
14 <https://doi.org/10.1175/JCLI-D-12-00502.1>
- 15 47. Westra, S., Fowler, H. J., Evans, J. P., Alexander, L. V., Berg, P., Johnson, F., et al. (2014).
16 Future changes to the intensity and frequency of short-duration extreme rainfall. *Rev.*
17 *Geophys.* 52, 522–555. doi: 10.1002/2014RG000464
- 18 48. Yatagai, A., Kamiguchi, K., Arakawa, O., Hamada, A., Yasutomi, N., & Kitoh, A. (2012).
19 Aphrodite constructing a long-term daily gridded precipitation dataset for Asia based on a
20 dense network of rain gauges. *Bulletin of the American Meteorological Society*, 93(9), 1401–
21 1415. <https://doi.org/10.1175/BAMS-D-11-00122.1>
- 22 49. Zhang, W., Villarini, G., & Wehner, M. (2019). Contrasting the responses of extreme
23 precipitation to changes in surface air and dew point temperatures. *Climatic Change*, 154(1–
24 2), 257–271. <https://doi.org/10.1007/s10584-019-02415-8>



25

26 **Figures:**



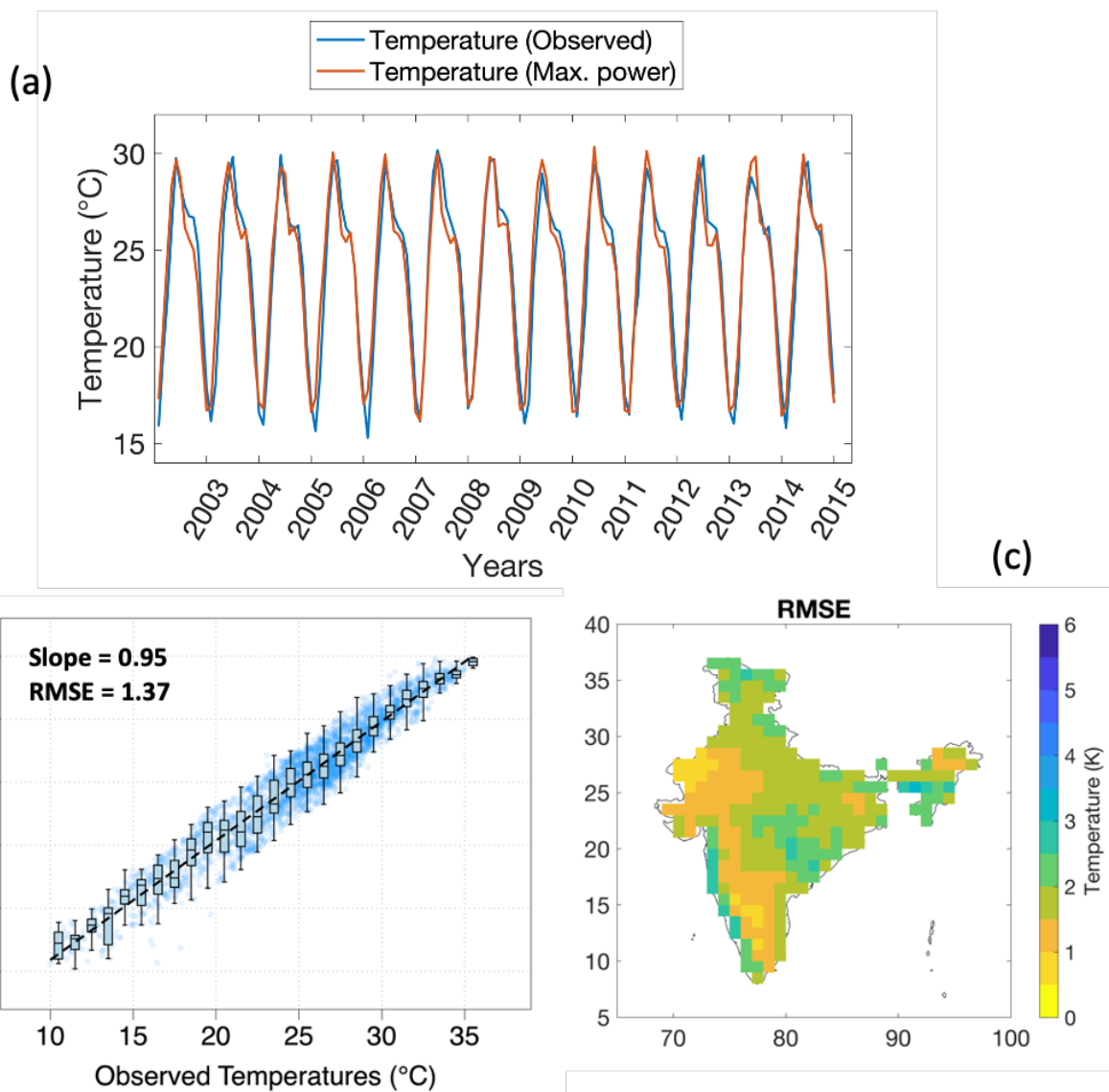
27

28 **Figure 1. Schematic diagram of the surface energy balance, the fluxes of solar (red) and terrestrial**
29 **(blue) radiation, as well as the turbulent heat fluxes (black). We consider turbulent heat exchange**
30 **being driven primarily by an atmospheric heat engine that operates at the thermodynamic limit of**
31 **maximum power.**

32

33

34

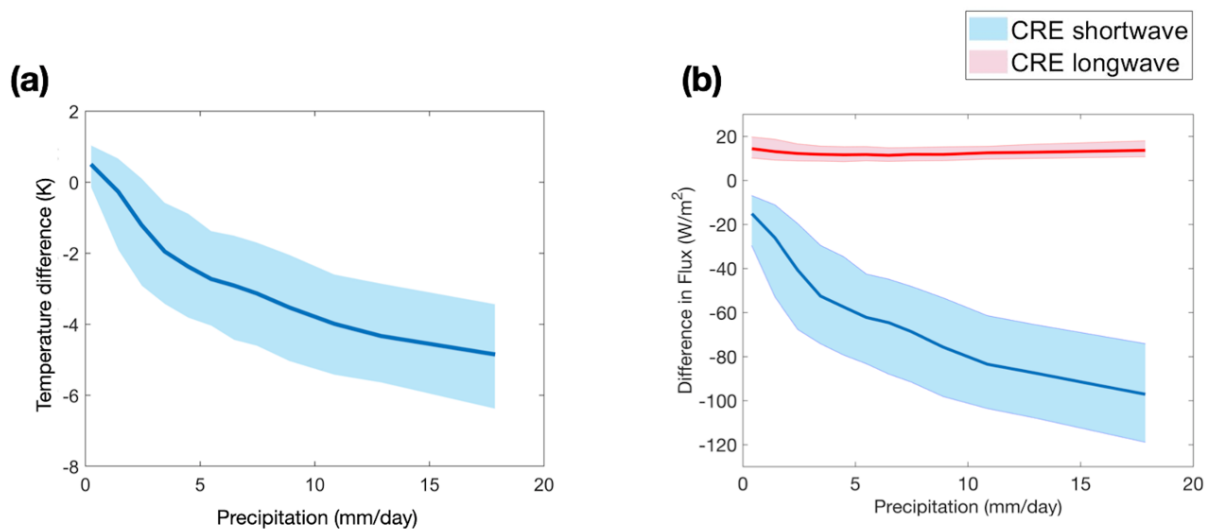


35
36 **Figure 2: Comparison of monthly mean temperature time series for observed (IMD) and estimated**
37 **“all-sky” surface temperatures, averaged over all grid points. (B) Regression between the two**
38 **temperatures at the grid-point scale. (C) Spatial variation of the root mean squared error (RMSE)**
39 **in temperature estimates from maximum power compared to observed temperatures.**

40



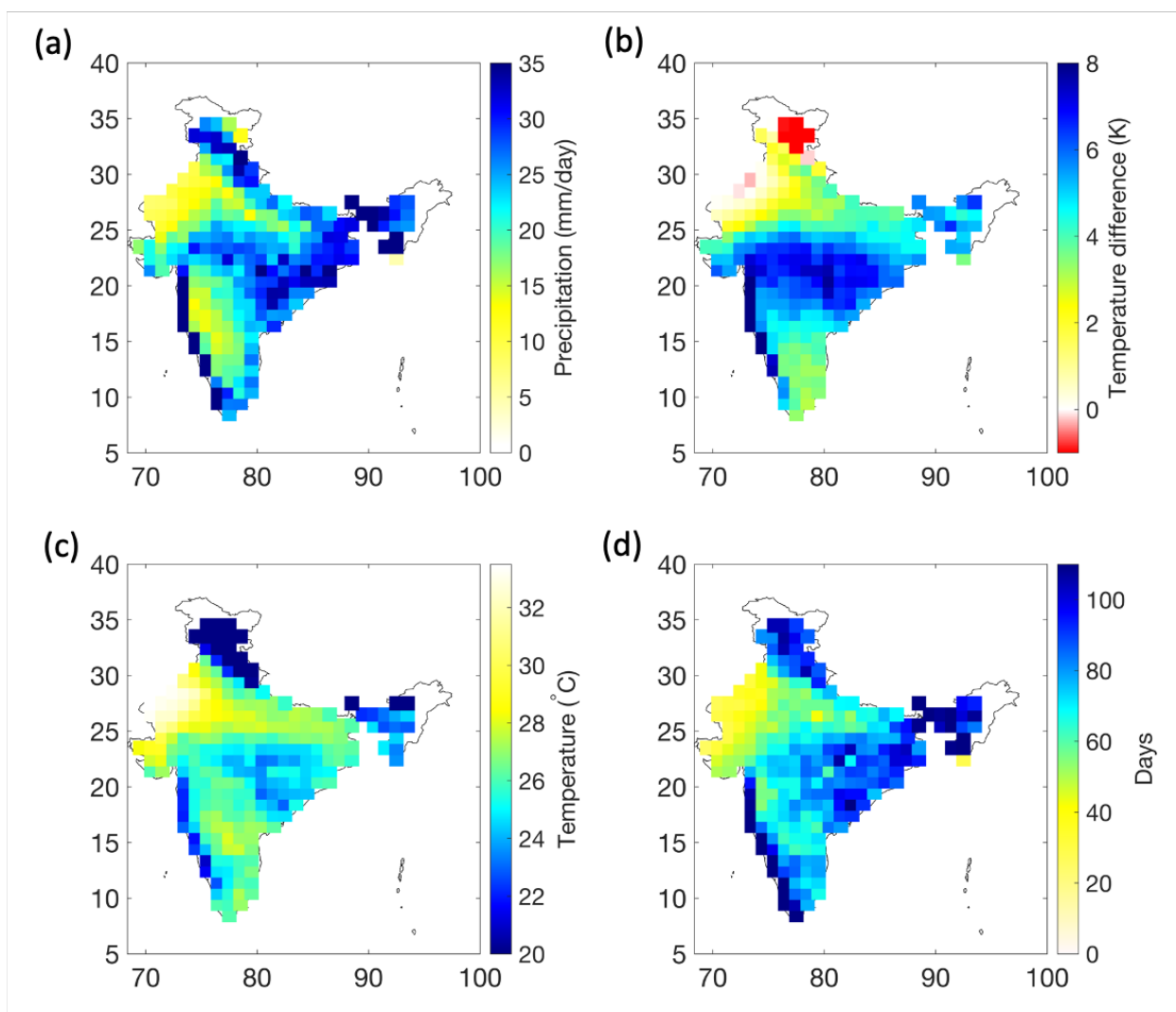
41



42

43 **Figure 3: (a) Cooling effect of clouds on surface temperatures calculated from the difference of "all-**
44 **sky" to "clear-sky" surface temperatures as a function of precipitation over the Indian region.**
45 **(b) Difference in net shortwave and downwelling longwave radiative fluxes ("Cloud Radiative**
46 **Effect", CRE) between "all-sky" and "clear-sky" radiative conditions at the surface as a**
47 **function of precipitation. This was inferred using NASA – CERES (EBAF ed4.1) dataset (Loeb**
48 **et al., 2018).**

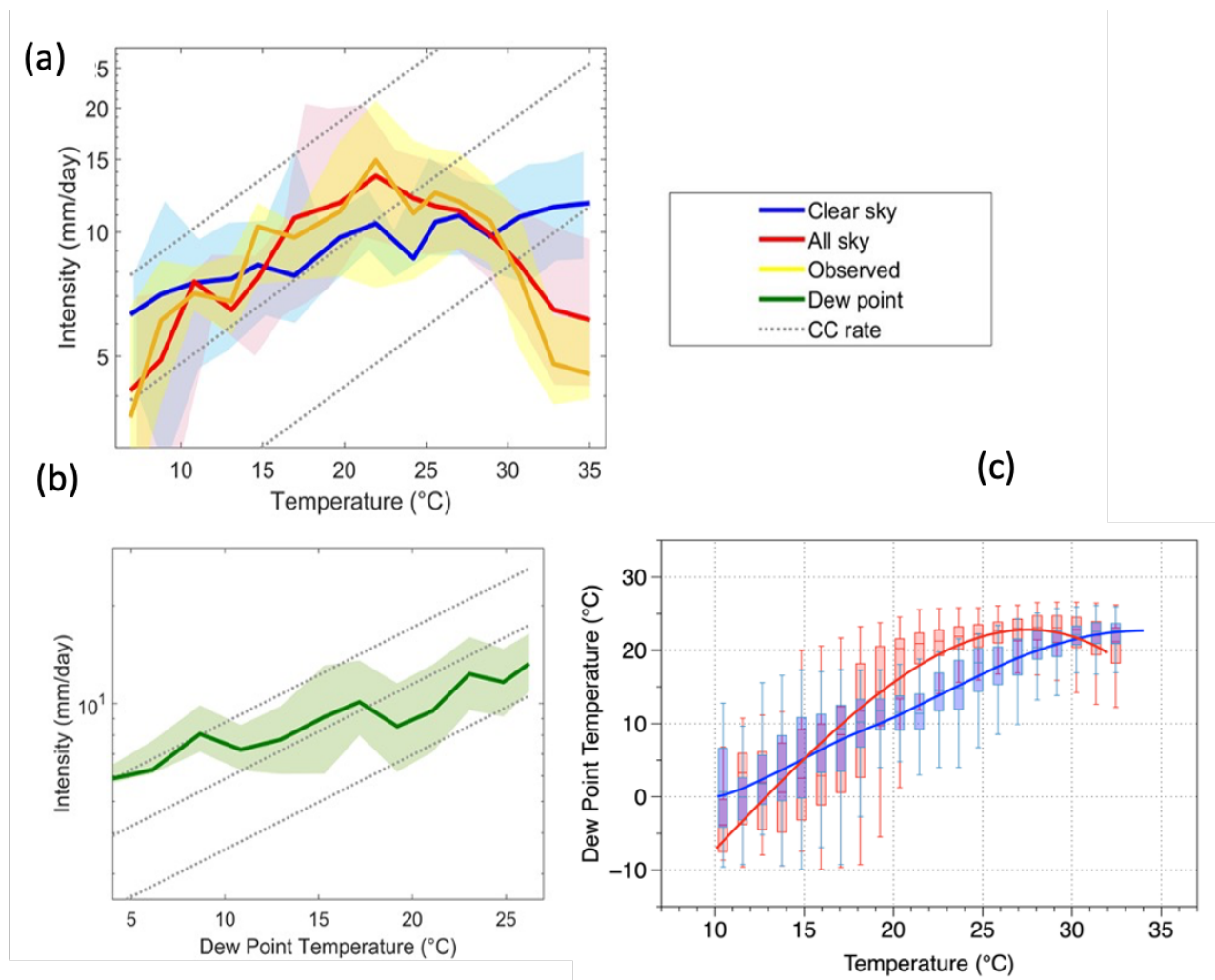
49



50

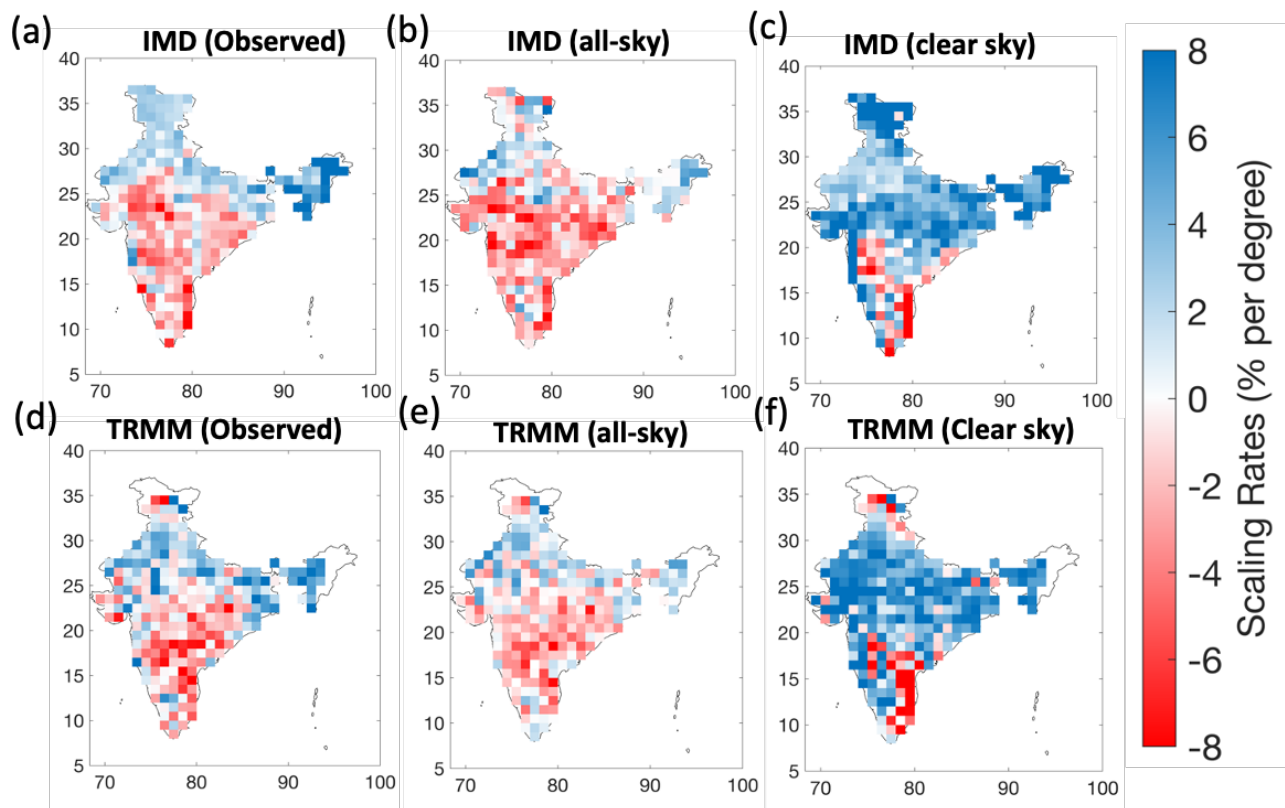
51 **Figure 4. Regional variation of (a) mean daily extreme precipitation (99th percentile) (b) the**
52 **temperature difference between "clear-sky" and "all-sky" radiative conditions averaged during**
53 **extreme precipitation events (c) "All-sky" surface temperature during the occurrence of the event**
54 **(d) Mean number of rainfall days per year**

55



56
57
58
59
60
61
62
63
64

Figure 5. (a) Extreme precipitation-temperature scaling using observed (yellow), "all-sky" (red) and "clear-sky" (blue) temperatures over India. (b) Same as (a), but using dew point temperatures. (c) Relationship between dew point temperatures and "all-sky" (red) and "clear-sky" (blue) temperatures. The shaded areas represent the variance in terms of the interquartile range for each bin. Grey dotted lines indicate the Clausius-Clapeyron scaling rate. Note: Logarithmic vertical axis for figure (a,b)



65

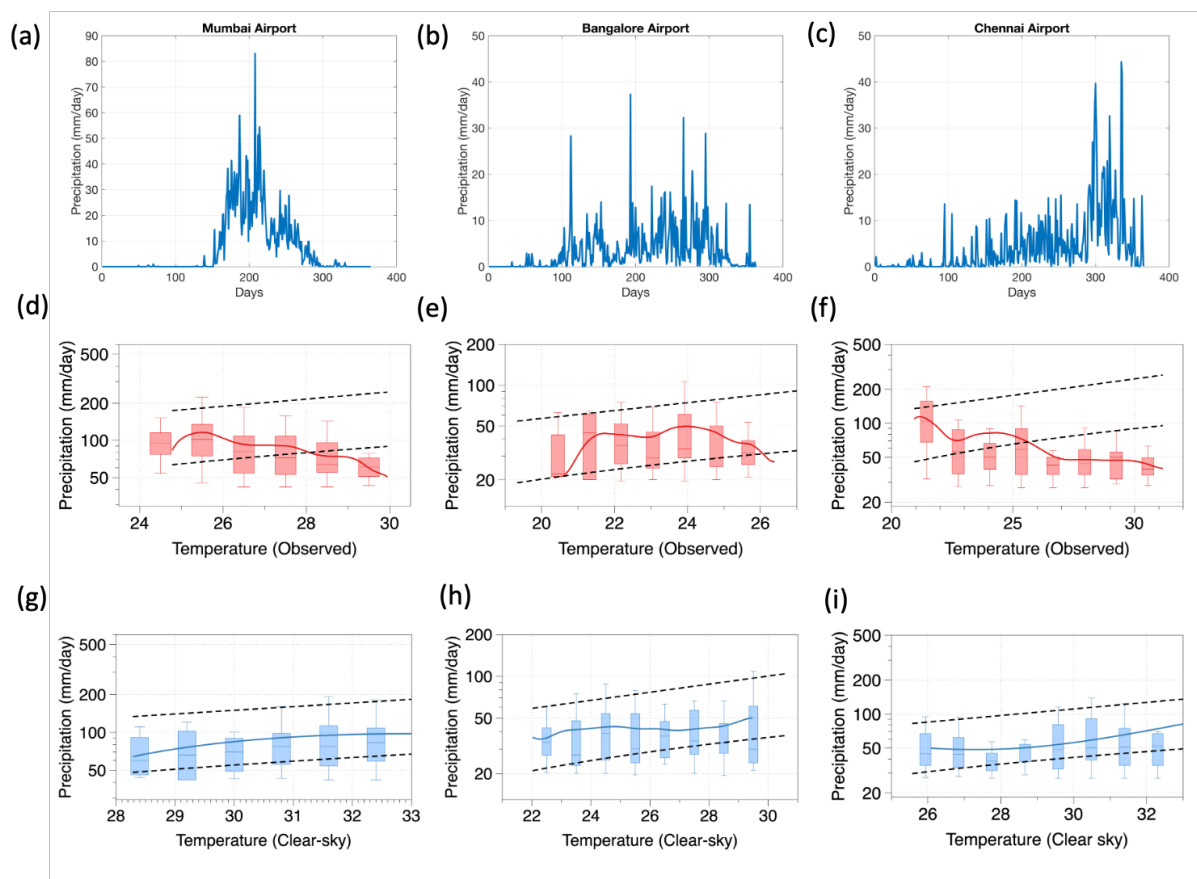
66 **Figure 6. Regional variation of 99th percentile precipitation-temperature scaling rates using daily**
67 **(a-c) and 3 hourly (d-f) rainfall data with observed temperatures (a, d), "all-sky" temperatures**
68 **(b, e) and "clear-sky" temperatures (c, f).**

69



70 **Appendix A: Validation of scaling results using station-based GSOD data**

71 We used three station-based daily observations from global surface summary of the day (GSOD) data
72 provided by National Oceanic and Atmospheric Administration (NOAA). We used the data at Mumbai,
73 Chennai and Bangalore Airport to produce the scaling curves (Appendix A). The choice of the station
74 was based to ensure the robustness of results using gauge data as well as to check the effect of seasonality
75 as the three sites receive rainfall during different period of the years. In Mumbai, rainfall occurs mainly
76 during the summer monsoon season while in Chennai heavy rainfall occurs during the winter months
77 (November and December). On other hand, Bangalore receives rainfall during both summer and winter
78 monsoon season (Fig. A1 a – c). Negative scaling was found over these three stations using observed
79 (yellow) and “all-sky” (red) temperatures while with “clear-sky” temperatures (blue), we find positive
80 rates largely consistent with the CC rate (Fig A1 d - i).



81

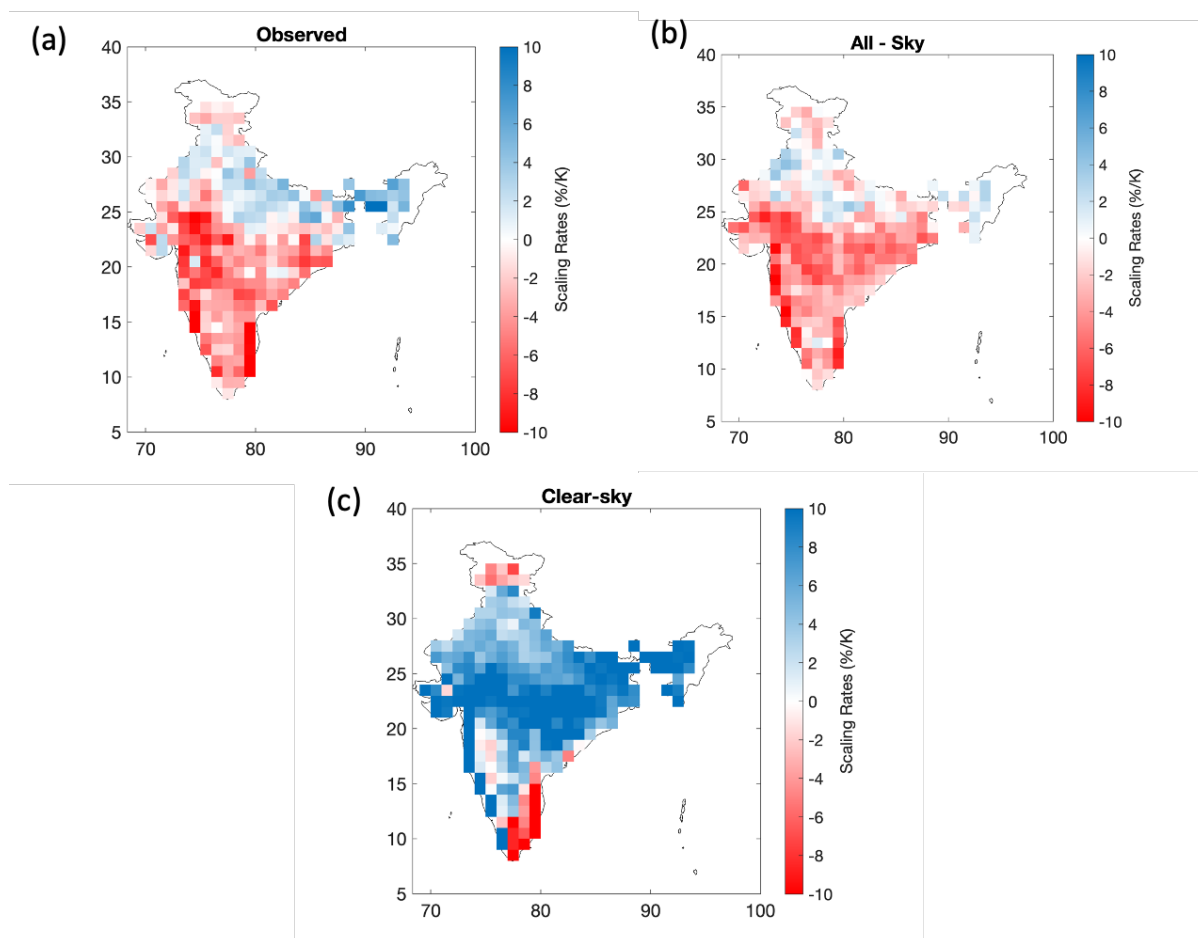
82 **Figure A1. (a-c) shows the annual cycle of mean daily precipitation over GSOD sites in Mumbai airport,**
83 **Bangalore airport and Chennai airport respectively. Extreme precipitation – temperature scaling curves for**
84 **(d-f) observed temperatures in red and (g-i) “Clear-sky” temperatures in blue are presented for all the three**
85 **sites. Red/Blue solid lines indicate the LOESS regression lines. Grey dotted lines indicate the Clausius-**
86 **Clapeyron scaling rate. Note Logarithmic vertical axis.**

87



88 **Appendix B: Validation of scaling results using APHRODITE dataset**

89 Figure B1 shows the spatial variation of daily precipitation – temperature scaling rates estimated from
90 quantile regression (similar to Fig. 6 in the main text) using the APHRODITE (Asian Precipitation –
91 Highly Resolved Observational Data Integration towards Evaluation of water resources) dataset (Yatagai
92 et al., 2012). The results show a diametric change in scaling from being negative for observed and “all-
93 sky” temperatures to coming close to CC rate (7%/K) for “clear-sky” temperatures. The findings were
94 consistent with that obtained using the IMD and TRMM dataset (Figure 6).



95

96 **Figure B1. Regional variation of 99th percentile daily precipitation-temperature scaling rates using (a)**
97 **Observed (b) “all-sky” and (c) “clear-sky” temperatures. Note: Precipitation data is from APHRODITE**

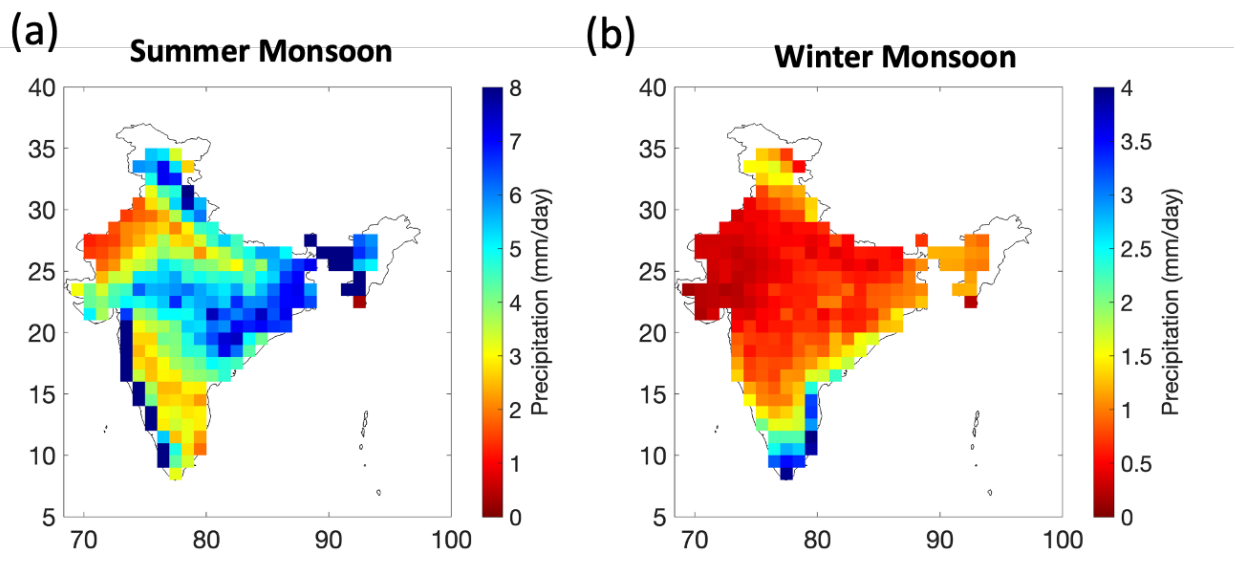


98

99

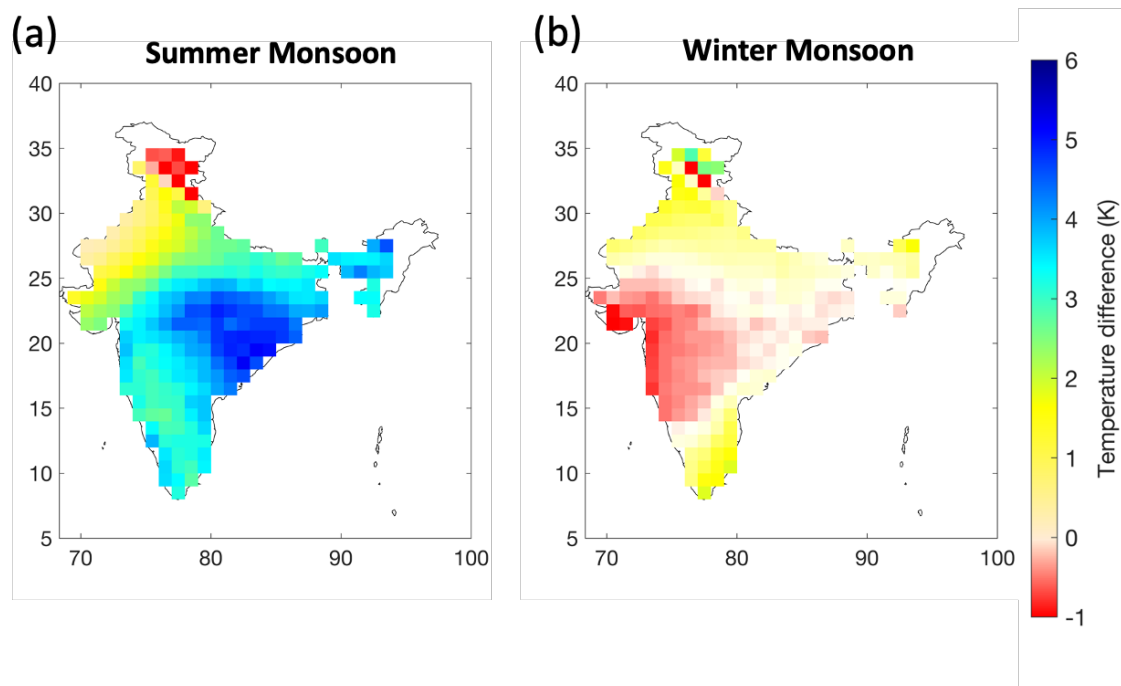
00 **Appendix C: Effect of seasonality on scaling rates**

01 To understand the role of seasonality on precipitation – temperature scaling. We divided the precipitation
02 period into two seasonal subsets i.e., summer monsoon season (April to September) and winter monsoon
03 (October to March). Season wise scaling curves (estimated using LOESS regression) are presented in
04 figure C3. We find that observed scaling is uniformly negative in summer over Indian region while during
05 winter the scaling is positive (Fig C3-a, d). This is not surprising because the “hook” or breakdown in
06 scaling happens at high temperature which leads to negative scaling in summer (Figure 5a). Reconstructed
07 “All-sky” temperature showed scaling pattern consistent with observations (Fig. C3- b,e). When scaled
08 with “clear-sky” temperatures, we observed a change in scaling for summer as it turns positive and come
09 close to CC rate. While for winter the scaling remains the same (already positive). It is also important to
10 note that almost 80% of total rainfall over India occurs during the summer monsoon season (Fig C1). As
11 a result, the cooling effect of clouds is mainly experienced during the summer monsoon (where we
12 observed a change in scaling) while the cooling effect remains less than 1K during the winter season (Fig
13 C2). Thus, one does not see a change in scaling between “all-sky” and “clear-sky” conditions for winter
14 season.



15

16 **Figure C1.** shows the map of mean daily precipitation during (a) summer monsoon (April – September) and
17 during (b) winter monsoon (October – March).



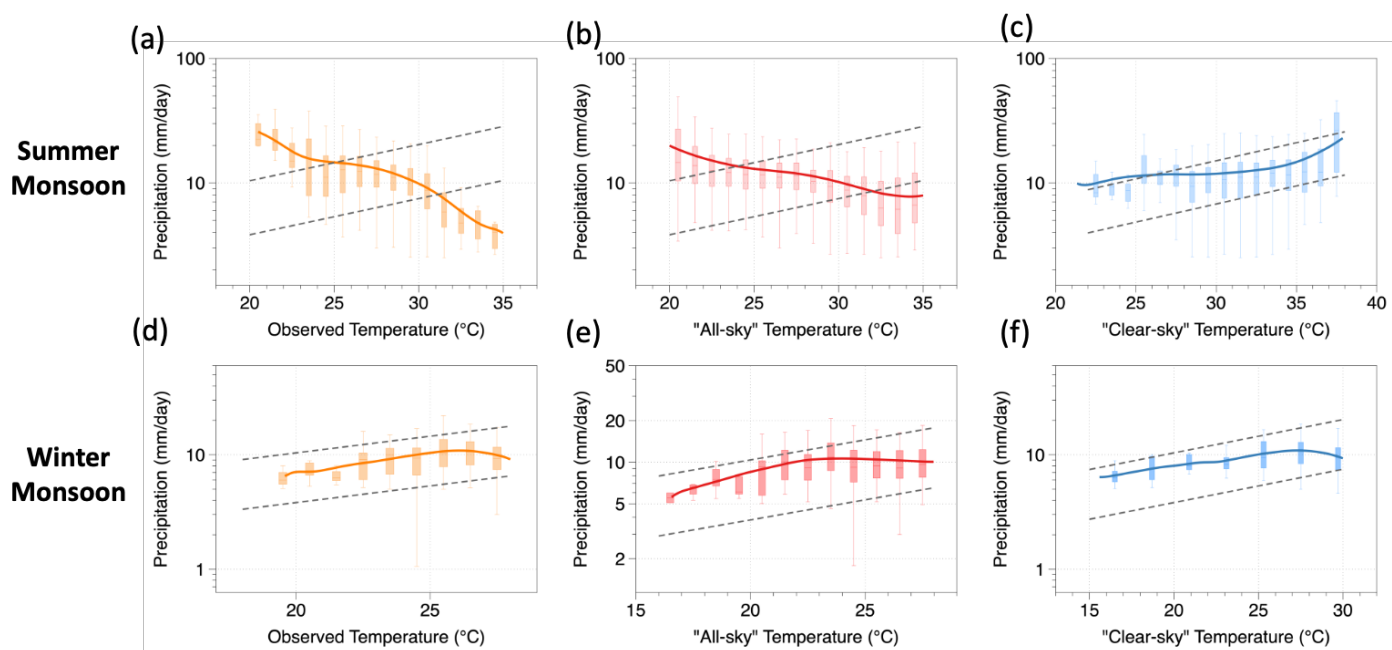
18

19 **Figure C2. Shows the map of cooling of surface due to clouds (defined as the difference between “clear-sky”**
20 **and “all-sky” temperatures) for (a) Summer monsoon (April – September) and (b) Winter monsoon**
21 **(October – March)**

22



23



24

25

26 **Figure C3. Extreme precipitation - temperature scaling during summer monsoon (a - c) and winter monsoon**
27 **(d-f). Scaling curves are shown in orange (a,d) for observed temperatures, in red (b,e) for “all-sky”**
28 **temperatures and in blue (c,f) for “clear-sky” temperatures. Orange/red/blue solid lines indicate the LOESS**
29 **regression lines. Grey dotted lines indicate Clausius – Clapeyron scaling rate. Note: Logarithmic vertical**
30 **axis. Dataset used is IMD.**